Raman spectroscopy of mini-CAST soot with various fractions of organic compounds: Structural characterization during heating treatment from 25 °C to 1000 °C

Le, Kim Cuong; Pino, Thomas; Pham, Van-Thai; Henriksson, Jonatan; Török, Sandra; Bengtsson, Per-Erik

Published in:
Combustion and Flame

DOI:
10.1016/j.combustflame.2019.07.037

2019

Document Version:
Peer reviewed version (aka post-print)

Raman spectroscopy of Mini-CAST soot with various fractions of organic compounds:

structural characterization during heating treatment from 25 °C to 1000 °C

Kim Cuong LE[1*], Thomas PINO[2], Van Thai PHAM[3,4], Jonatan HENRIKSSON[1], Sandra TÖRÖK[1], Per-Erik BENGTSSON[1]

[1]*Division of Combustion Physics, Department of Physics, Lund University, Lund, Sweden*

[2]*Institut des Sciences Moléculaires d'Orsay, Univ Paris Sud, Université Paris-Saclay, Orsay, France*

[3]*Advanced Functional Materials for Energy and Environmental Applications Research Group, Ton Duc Thang University,Ho Chi Minh City,Vietnam*

[4]*Faculty of Applied Sciences, Ton Duc Thang University, Ho Chi Minh City, Vietnam*

[*] Corresponding author:

E-mail address: thi_kim.cuong_le@forbrf.lth.se (Thi Kim Cuong Le)

Postal address: Department of Physics, Combustion Physics, Lund University, Box 118, SE-221 00 Lund, Sweden

Telephone number: +46 46-222 93 60

Abstract

Soot particles undergo considerable changes in composition, morphology, as well as in internal structure during formation from the incipient particles to more mature aggregates, and still there is a lack of understanding of these mechanisms. In this study, soot produced by a mini-CAST soot generator was probed using Raman spectroscopy with focus on soot with large variation in size and fraction of organic compounds. The volatility of organic compounds and changes in internal bonding structures of the soot was surveyed by heating the samples from room temperature up to 1000 ^{o}C in a flow of inert N_2 gas. The soot rich in organics showed more complex Raman spectra and stronger photoluminescence background. In particular, Raman signatures interpreted as the C-H "out-of-plane" mode, ethers C-O-C, and carbonyl C=O groups were observed. During the heating treatment, these signatures disappeared, which was related to vaporization of the organics. Moreover, an enhancement of Raman band intensity of mature soot during heating treatment was observed for the first time. Our study thus brings new information on structural and compositional changes for soot during heating treatment in an inert atmosphere.

Keywords

Raman spectroscopy, soot, organic compounds, thermal treatment

1. Introduction

Soot formation in combustion is a complex process involving gas phase chemical kinetics, heterogeneous reactions on the particle surface and particle dynamics [1–3]. Hence size, morphology, internal structure, and optical properties of soot depend on various parameters in the combustion process such as the fuel, type of combustion process as well as the reaction time and temperature history [4–9]. Soot particles appear as clusters or aggregates containing few to hundreds of primary particles [10–12]. In the recent decade, many studies have revealed soot particle sizes from 1 to 3 nm in diameter for nascent soot particles [2,13,14] and 10 to 50 nm for primary particles in mature soot [10,15–18]. Mature soot particles are more turbostratic and have a higher level of structural order compared to smaller nascent particles [7,10,19–27]. The nascent soot and the mature soot have

significantly different properties, appearances and internal nanostructures. The surface of nascent soot is demonstrated to be more reactive than that of mature graphitized soot [28,29]. Using high-resolution transmission electron microscopy (HRTEM), the primary particles of mature soot exhibit an inner core surrounded by an outer shell consisting of concentric graphene sheets (also called polyaromatic units) parallel to the particle surface [30,31]. While the outer shell is composed of polyaromatic units more or less stacked, the inner core appears as reminiscent soot nuclei which may be amorphous [16,17,31]. The structures of immature soot are much more disordered with shorter and potentially highly curved fringes without a core-shell type of structure. On the particle surfaces, organic matters including polycyclic aromatic hydrocarbons (PAH) are adsorbed [32,33]. These volatile and semi-volatile compounds may significantly influence the optical, chemical and physical properties of the soot.

As the chemical and physical soot properties have big impacts on climatological and health aspects, it is important to characterize the composition and structure of various types of soot. Previous studies have shown that a mini-CAST soot generator can produce soot within a range of sizes and optical properties, and this device has been widely used for soot characterization and as a calibration source [34–39]. Through changes of the operating conditions of the mini-CAST, various types of soot can be produced from brownish small soot particles with high organic content to larger black soot particles with low organic content. The choice of operating conditions thus influence on soot optical as well as chemical properties [34,36,37]. In particular, it was shown that some operating points produced soot with substantial fractions of organic compounds (OC) and polyaromatic hydrocarbons (PAHs) [21,34,35]. In our investigations on a miniCAST soot generator [21,34], we use the term “soot” for the carbonaceous aerosols produced by this device. The soot thus is any black, blackish or brown particles containing more or less graphite-like structural particles and organic materials which could be either internally or externally mixed [40].

In previous studies, we focused on investigations of composition, morphology and nanostructure of soot, and their relations to the absorption coefficient using online soot particle aerosol mass

spectrometry (SP-AMS), thermal-optical analysis, HRTEM, and multi-wavelength extinction [21,34]. In these works, we showed that we could produce soot with characteristic properties similar to immature soot (OP7 soot) and mature soot (OP1 soot). These types of soot have also been studied in this work. Beside our published works, other fruitful results on properties on mini-CAST soot are, for example, on the effective particle density [35,41,42], the chemical structure, size and morphology on soot optical properties [38,42] and evaporation/transformation/oxidation of organic components [37]. Yet, there is missing information on the internal bonding structures of soot and chemical properties of OC as well as their possible connection with graphenic structures. These features will be emphasized in this work via Raman spectroscopy. The heat treatment at stepwise higher temperatures (up to around 1000 ^{o}C) leads to structural changes for the soot, and as the measurements are performed in an inert N_2 atmosphere, oxidation processes are avoided. The heating process also leads to an interesting thermal effect on the Raman band intensities.

2. Analysis of Raman spectra of soot

Raman spectroscopy has high potential for analysis of soot nanostructures and is sensitive to chemical bonds and vibrational frequencies of molecules and polyaromatic units. The spectral region 1000-1800 cm^{-1} provides information on carbon organization such as bonding structures and size of the aromatic domains, as later shown in Fig. 3. The most prominent features are the so-called *D* and *G* bands, which lie at around 1350 and 1590 cm^{-1}, respectively. The *G* peak was originally assigned to an ideal graphitic lattice vibration mode with E_{2g} symmetry in the crystalline structure of graphite [43]. In non-crystalline carbons, this mode occurs at all sp^2 pairs and does not require the presence of sixfold rings [44,45]. The *G* band in the Raman spectra is characteristic of sp^2 carbon networks. It dominates the Raman spectra because of resonance effects [46]. The *D* peak appears at about 1350 cm^{-1} and corresponds to a breathing mode of A_{1g} in a graphitic lattice vibration. This mode is forbidden in perfect lattice but becomes active with the presence of defects occurring at the edge of the planes of the graphene sheets [44,47,48]. Its intensity is strongly related to the presence of sixfold aromatic rings [45]. The detailed analysis of *D* and *G* bands reveals the presence of several bands. It

was thoroughly presented by Sadezky *et al.* (2005) and their nomenclature is used thereafter, for instance the *D* band is called D_1 after detailed spectral decomposition to take into account the other defect induced bands. Another first-order band accounting for structural disorder is the D_2 peak at ~ 1620 cm^{-1} that can be observed as a shoulder of the *G* band. It is generally assigned to an aromatic C=C stretching mode in polyaromatic units not belonging to a basic structural unit (BSUs are stacked polyaromatic units) [49,50] or at BSU surface and also to the variation of the distance between the graphene units [44]. The frequency of D_1 and D_2 modes shift to higher energy with increasing excitation energy [51,52] and these two peaks are defect-induced Raman features which appear as the number of defects increases. There is also a contribution of a very broad D_3 peak at ~ 1500 cm^{-1} originating from the amorphous carbon fraction of soot (sp^2 fraction of the amorphous network). The amorphous carbon component is a complex mixture of sp^2 and sp^3 bonded carbon atoms with no local order and ion impurities [38,51,53] and the feature traces the internal vibrational modes in small aromatic units related to asymmetric breathing of the carbon rings and C=C stretching of internal and edge carbons [33]. In addition, the D_1 band may exhibit a shoulder peak at ~1180 cm^{-1} which we label as D_4 [38,54,55]. It could come from sp^3 and intermediate $sp^2 – sp^3$ hybridization states [56] of carbon atoms or C–C and C=C stretching vibrations of polyene-like structures [57,58]. The mixed $sp^2 – sp^3$ hybridization is possibly caused by curved PAH layers. They can also originate from defects found within the polyaromatic unit such as non-hexagonal rings or vacancies, or found between the polyaromatic units and forming the cross-linkage with carbon chains [38]. It is noteworthy that the spectral decomposition and assignment of the Raman spectra of disordered carbons is still under debate with some recent works proposing another interesting viewpoint of the band profiles [5,59–63]. Here we have chosen to rely on the Sadezky *et al.* (2005) approach for comparison with previous work but more importantly to focus our attention on the new features of the organic compounds that were not taken into account up to now. One additional peaks (D'_1) at ~1270 cm^{-1} was also observed in Raman spectra of rich organic soot. This peak indicates the contribution of organic compounds [37,55] but its origin is still ambiguous [37,64,65]. It could arise from the merging of sub-bands

characteristic of the individual polyaromatic subunits [55,66]. Recently, the online Raman spectroscopy of aerosol soot produced by ethylene/oxygen flame at low pressure pointed out the existence of sp hybridization states in the 1800-2100 cm^{-1} spectral region [67]. This spectral region is well-known as the Raman fingerprint of sp hybridized carbon atoms, either with alternating triple and single bonds (polyyne -C≡C-) or with only double bonds (polycumulene =C=C=). Having spectroscopic information is clearly relevant and Raman spectroscopy is a very powerful tool to characterize soot chemical and structural properties of the carbonaceous structure and the organic compounds.

3. Experiments

A mini-CAST 5201C soot generator (mini-CAST Jing Ltd.) was used to produce the soot nanoparticles [34]. In this generator, a co-flow propane-air diffusion flame is quenched at a fixed height with N_2 gas resulting in a gas stream containing soot particles. The quenching gas prevents the soot particles from further combustion and restricts further reactions in the particle stream at ambient air condition. Soot with various characteristics were achieved by changing the flame operating conditions (OP), detailed in Table 1, from small soot particles with high organic fraction (OP7) to larger aggregated soot particles with low organic fraction (OP1) [21,34]. From optical property and morphology point of view, soot produced at OP1 and OP3 are very similar, and data from the OP3-case are not shown in this paper. When changing the settings towards higher OP by diluting the fuel with nitrogen, the flame temperature is reduced as well as earlier stages in the soot formation process are quenched [21].

At each OP, the sapphire windows were inserted in front of the exhaust pipe of the miniCAST soot generator to collect soot particles. While OP1 and OP5 soot needed 17 – 30 minutes for preparing each sample, OP6 and OP7 soot required 1 – 2 hours. These thin soot films were then heated at temperatures between ambient and 1000 ^{o}C by a LINKAM (TL1200) heating stage. A measurement series consisted of heating a soot sample to successively higher temperatures. After reaching each

elevated temperature, the sample was kept at this temperature for one minute. Then the soot was cooled fast to room temperature, after which the Raman measurement was performed. The soot was then heated to the next higher temperature. The procedure was repeated until the soot signal disappeared and signal background from the sapphire window appeared in the spectra. The temperature at which the soot films disappear are 1000 ^{o}C for OP1 soot and 800 ^{o}C for OP5, OP6 and OP7 soot.

N_2 continuously flowed at a rate of 50 ml/min through the LINKAM system during heating. Thus deposition of evaporated species from the soot on the observation window of the LINKAM could be avoided. In addition, in this inert atmosphere oxidizing reactions of the soot structures could be prevented.

Table 1. Burning conditions and characteristics of soot at different operating points.

OP	Propane ($Lmin^{-1}$)/oxidation air ($Lmin^{-1}$)/N_2 mixing gas ($Lmin^{-1}$)	N_2 quenching gas ($Lmin^{-1}$)	Dilution flow ($Lmin^{-1}$)	OC/TC [34]	(OC+PC)/TC [34]	PAH/TC [34]	Fringe length (nm) [21]	Fringe tortuosity (nm) [21]	GMD (nm) [21]
1	0.06/1.55/0	7	0	9%	9%	0.009%	~ 0.61 ± 0.02	~1.18 ± 0.01	310
5	0.06/1.47/0.2	7	0	12%	18%	0.6%	0.56 ± 0.01	1.20 ± 0.02	200
6	0.06/1.42/0.25	7	0	32%	59%	3.9%	0.54 ± 0.02	1.21 ± 0.01	130
7	0.06/1.36/0.3	7	0	53%	87%	5.5%	0.499 ± 0.01	1.23 ± 0.01	80

OC, Organic Carbon; PC, Pyrolytic Carbon; TC, Total Carbon; PAH, Polycyclic Aromatic Hydrocarbon; GMD, geometric mean diameter of the aggregate size distributions.

Raman spectra of the heat-treated soot were recorded by our homebuilt Raman spectrometer shown in Fig. 1. The heating device was combined with our Raman experimental setup to ensure the same sample probe surface and position during the measurements. An unpolarised diode laser beam at 532 nm was directed vertically through a hole in a mirror placed at 45 degrees, and focussed using a lens (Φ = 25.4 mm, f = 30 mm) to obtain a maximum power density of 6×10^3 mW/mm^2 at the focused point on the soot samples. A power density dependence of the Raman spectra was measured to make sure that no thermal/irradiation damage occurred in the soot structure at this excitation power. The backscattered photons were collimated using the same lens (Φ = 25.4 mm, f = 30 mm), and reflected

by a broadband mirror and focused onto the entrance of a round-to-linear fiber optic bundle (Thorlabs BFL200HS02) by a lens (Φ = 25.4 mm, f = 150 mm) to match the numerical aperture of the spectrometer. This fiber bundle contains 7 fibers arranged in a circular configuration (round) at the entrance and a line configuration (linear) at the end. The linear end was coupled with the slit of a spectrograph (IsoPlane SCT320, Princeton Inst.) connected with an ICCD camera (PI-MAX IV, Princeton Inst.). The spectral resolution of the setup was ~ 12 cm^{-1}. Notice that a long wave pass edge filter (Thorlabs, FEL0550) and a notch filter (Thorlabs, NF533-17) were inserted in front of the focussing lens to cut off the elastic scattering and the anti-Stokes region. In addition, a short pass filter with cut-off wavelength at 650 nm was also inserted in front of the focussing lens to avoid the photoluminescence from the ceramic cup (Al_2O_3) of the LINKAM [68]. For each sample and temperature, 5 spectra with recording time of 7 min each were averaged for achieving satisfactory signal-to-noise ratio.

4. Results and discussion

4.1. Raman spectra of non-heat treated soot varying from poor to rich organic contents

Figure 2a displays Raman spectra superimposed on photoluminescence signals of four non-heat treated soot samples named OP1, OP5, OP6 and OP7 spanning from larger particles of mature character to smaller soot particles of immature character[34]. In Fig. 2b the same Raman spectra are shown after subtracting the photoluminescence contribution using a second-order polynomial function [5,38,51,67,69–71] in the spectral region from 800 cm^{-1} to 2320 cm^{-1}. From OP7 to OP1, the slope of the photoluminescence background decreases significantly indicating that the hydrogen content (H/C atomic ratio) becomes lower [5,72,73]. The H/C ratio of soot decreases during aging in a flame and accompanies the soot evolution towards a more turbostratic organization [7,74]. The lower H/C ratio is associated with a lower number of active C-H sites and leads to a change of electronic structure via the increase of sp^2/sp^3 hybridization ratio and/or the increase of graphenic planar structure. This fact is consistent with the increase of soot maturity in our previous study when

changing conditions from OP7 to OP1 [21,34]. The photoluminescence arises from a large fraction of organic carbon including PAHs prevailing in such fuel-rich flames [36,71]. Particularly, while four aromatic ring PAHs (m/z 202) dominate in the total particulate PAH mass in OP1 soot, larger 4, 5, and 6 aromatic ring PAHs (m/z 226-300) are ascendant in OP5, OP6 and OP7 soot [21]. PAHs containing more than five aromatic rings and condensed species are known to fluoresce in the visible range [71,75,76].

The 800 - 2320 cm^{-1} Raman spectral region shown in Fig. 2b exhibits all common bands of soot summarized in the introduction and in Table 2 the observed bands for our miniCAST soot are listed. The first main observations are that the more mature OP1 soot mainly exhibits the common D and G peaks for carbonaceous material. From OP1 to OP7 soot, the spectral diversity increases, which can be related to a higher OC content. For increasing OP values the OC content is higher, as shown in Table 1. It is thus shown that the higher the OC content is, the stronger *D'1* shows up. Moreover, some additional peaks at ~ 900 cm^{-1} (denoted as *B* band) and at ~ 1980 – 2200 cm^{-1} (called *C* band) also follow this trend. Such signals have not yet been reported for deposited soot. Although observed in previous studies (Fig. 4 in ref [51] and Fig. 1 in ref [58]), the *B* and *C* bands were not taken into account in their evaluations.

Comparing to *G* peak area, that of *B* peak gives negligible contribution for OP1, and increases from OP5 to OP7. The *B* band position is very close to the B_{2g} mode (~ 867 cm^{-1}) observed in the polarized Raman spectra of highly oriented pyrolytic graphite (HOPG) and pyrolytic graphite (PG) due to "out-of-plane" atomic displacements [48,77,78]. As a consequence, no Raman active zone-center mode is expected with the "out-of-plane" displacements, but this B_{2g} mode becomes Raman active by change of crystalline point symmetry caused by the discontinuity of graphene layers [77]. Our *B* band position is also close to the B3 band position in Fig. 1b of the ref. [73] related to C-H "out of plane" bending vibrations of polyaromatic hydrocarbon molecules recorded in amorphous carbon layers [73,79]. It should be reminded that the existence of our *B* band is pointed out in un-polarized Raman

measurements and strengthens with the increase of PAH amount on the soot particle surfaces. The C-H "out-of-plane" displacement in soot particles whose Raman spectra are similar to ours was also identified via infrared spectroscopy in ref. [55]. These clues thus strongly support for the vibration of C-H bonds of PAHs considered as the origin of the *B* band in our spectra.

Being absent in the Raman spectrum of OP1, the *C* band emerges in the Raman spectra of OP5, OP6, and is pronounced in that of OP7. As mentioned in the introduction, this spectral region indicates the "out-of-phase" stretching mode in linear all-carbon chains [80,81], in which the cumulenic chains (1800-2000 cm^{-1}) [80,82,83] were demonstrated to be less stable than the polyynic chains (~2000-2200 cm^{-1}) [81,84–86]. There is a very weak cumulenic chain signal observed in our spectra. The *C* peak position at ~2145 cm^{-1} is mostly caused by the polyynic chains probably involved in the organic condensed materials. The linear all-carbon sp linkages sometimes occur in organic molecules [87] and the polyyne chains are quite stable in air at room temperature [83]. Ravagnan et al. reported that N_2 does not chemically interact with the sp chains whereas oxygen reacts with the carbynoids species causing their fast and almost complete destruction [85]. This argument may explain the absence of sp bonds in the Raman spectroscopic study by Ess *et al.* [37], where there soot samples were studied in a flow of air during heating.

In the 1000 – 1300 cm^{-1} spectral region of rich organic soot, D_4 (~1180 cm^{-1}) and D'_1 (~1270 cm^{-1}) peaks are often mentioned [37,38,55,64,88,89]. However, the existence of a peak at 1060 cm^{-1} in previous studies, such as Fig. 2 in ref [89], Fig. 5 in ref [88], Fig. 7 in ref [37], and Fig. 2a in ref [64], has not been explained yet. Two peaks at 1060 and 1750 cm^{-1} are observable in the OP6 and OP7 Raman spectra, which presumably originate from the stretch vibrations in oxygen involving C-O-C ether bonds and carbonyl C=O [55,64]. While C-O-C peak appears for all OP cases, the C=O peak is only observable in OP6 and OP7 soot. The oxygenated groups are located in the organic compounds according to the later presented analysis of our data. These Raman features were observed by Liu et al. [64], in which the stretching vibrations of C-O groups and carbonyl groups originates from lactone,

anhydride and ketone species formed via ozonization reactions of soot. It is interesting that our oxygenated hydrocarbon observation is highly consistent with Johansson *et al.* [90], in which most oxygenated species seen in their flames were furans (an ether in a 5-membered ring) and that C-OH was the furan precursor [90]. Through the computational and experimental approaches, they discovered that oxygen addition to PAHs occurs mainly via reactions with OH and O_2 and be integral to the molecular-growth pathways leading to soot formation as well as to OC coating of soot particles in the combustor and in the atmosphere [90]. Last but not least, these oxygen functional groups also can be formed spontaneously at the surface of soot by exposure to the atmosphere [91] during the sampling process.

Table 2: Summary of the first order Raman spectral indicators for mini-CAST soot

Position (cm^{-1})	**Peak**	**Origins**	**References**
870 - 900	B	C-H "out of plane" bending vibrations of polyaromatic hydrocarbon molecules recorded in amorphous carbon layers	[73,79]
1060	Ether (C-O-C)	Oxygenated hydrocarbon species - Stretching vibration of ether group (C-O-C)	[64,90]
~ 1180	D_4	sp^3 and intermediate sp^2-sp^3 hybridization states of carbon atoms or C-C and C=C stretch vibrations of polyene-like structures	[38,56–58]
~ 1270	D'_1	Could be the merging of sub-bands characteristic of individual polyaromatic subunits in organic compounds	[55,64,65,92]
~ 1350	D_1	Breathing mode of A_{1g} in a graphitic lattice vibration	[44,47,48]
1500	D_3	Amorphous carbon (a complex mixture of sp^2 and sp^3 bonded carbon atoms)	[38,45,51,53]
1590 - 1625	G	C=C stretching modes of either aromatic rings or olefinic chains	[43,93]
1750	Carbonyl (C=O)	Oxygenated hydrocarbon species - Stretching vibration of carbonyl group (C=O)	[64,90]
1800 - 2000	C_1	sp hybridization state: Polycumulene (=C=C=)	[67,80,82,83]
2000 - 2200	C_2	sp hybridization state: Polyyne (-C≡C-)	[67,81,84–86]

The fitting model for spectral deconvolution

We proposed a fitting protocol for the spectral deconvolution based on the above discussion. Figure 3 shows the spectral deconvolution applied to non-heat treated OP6 soot. The model is based on Sadezky's model [51] (4 Lorentzian (L) and one Gaussian (*G*) bands) with addition of one Lorentzian band (D'_1) at 1240 cm^{-1}, and 5 Gaussian bands at 870 cm^{-1} (B band), 1060 cm^{-1} (C-O-C band), 1750 cm^{-1} (C=O band), 2050 cm^{-1} (C_1), and 2145 cm^{-1} (C_2). It should be taken into account that G and D_2 peaks were well fitted by one Breit-Wigner-Fano (BWF) peak instead of separating into *G* and D_2 peaks. Previous studies have also put in evidence the arbitrary nature and the difficulties in separating *G* and D_2 peaks [5,59,60,94]. Therefore, the effort to decompose D_2 from *G* peak in our samples is unproductive. A single peak was then substituted, in which asymmetric BWF line shape is selected because of its better goodness-of-fit (larger aR^2) and the closer position of fitted *G* peak to the band maximum of the *G* peak from the spectra. This BWF function provides an effective representation of the asymmetric broadening of the *G* peak [5,46]. In summary, the fitting model used in this work is a combination of three Lorentzian peaks (D_4, D'_1, D_1), 1 BWF ($G+D_2$) and 6 Gaussian peaks (*B*, C-O, D_3, C=O, C_1 and C_2) as presented in Fig. 3. The positions of D_4, D'_1, D_3, and the ether and carbonyl bands are fixed at 1180, 1245, 1500, 1060 and 1750 cm^{-1}, respectively. More details of the deconvolution treatment are clarified in the supplementary material. *Notice that in the rest of the paper, the term G is used to refer to the combination peak of G and D_2 peaks.*

4.2. The internal structural evolution of soot heated in N_2 environment

Raman spectroscopy of soot from heat treatment in N_2 gas allows us to study soot structural changes and volatility of organic compounds without oxidation processes. The first column of Fig. 4 shows the spectral evolution of the four soot samples heat-treated in N_2 from ambient temperature to the temperature at which their Raman spectra of soot vanishes. As an insert in each of these graphs, a photo of the sampled soot for each case is shown before heat treatment. It clearly shows that OP1 soot has a black colour, whereas the colour turns more brownish for OP5, OP6, and especially OP7 soot. In Fig. 4, the Raman and photoluminescence signals evaluated in the range of 800 – 2320 cm^{-1}

are shown. It should be recalled that the photoluminescence background is subtracted from the observed signal with a second order polynomial function. Figure 5 compares the Raman spectral variation of non-heat treated soot and heat-treated soot at 600 ^{o}C for the four OP cases, and deconvolution of the data in Fig. 4 leads to the results in Fig. 6. This figure shows, as discussed later, the disappearance of non-aromatic vibrational bands as a function of temperature. There is a clear correlation of the decrease of photoluminescence signal with increasing heating temperature shown in Fig. 4 and the disappearance of *B, C, D_1'* and oygenated groups in Fig. 5 and Fig. 6. The existence of "out-of-plane" C-H, hybridized bond chains, polyaromatic subunits and oxygenated groups may thus mainly originate from organic compounds and within the cross linkages between polyaromatic units [49].

Organic compound reduction by heat treatment

The photoluminescence intensity from OP5, OP6 and OP7 soot shows a decrease with increasing heating temperature. For the soot rich in organics, the vaporization/transformation of OC by increasing the heating temperature decreases the photoluminescence intensity. For OP1 soot, which contains the lowest amount of organic compounds, an increase of the background is observed. On the one hand, this upward trend is contributed by the increase of signals from the sapphire window indicated by the increase of the sapphire sharp peaks at 749 and 892 cm^{-1}. On the other hand, the photoluminescence of OP1 soot also slightly increases which could trace a decreasing defect density with heat treatment that favour radiative relaxation [95].

In Fig. 4, the black spectrum in the upper panel shows a spectrum from the sapphire window after heat treatment. The Raman signals were gradually lost when heating the samples to elevated temperatures and signals from the sapphire substrate showed up instead. This occurred at around 1000 °C for OP1 and 800 °C for OP5-7. Visual inspection of the sapphire windows after this heating process showed absence of the soot film. At least a partial explanation could be that oxidized surface groups such as carbonyl groups act as active sites for the oxidative dehydrogenation and are thermally

decomposed releasing CO and/or CO_2 and in some cases H_2O and H_2 [91]. In Matuschek et al.'s study [96], a thermal desorption of soot accounts for more than 10% of the particle mass up to 800 °C. The experimental condition consisting of a small nitrogen flow at atmospheric pressure could also influence on the disappearance of the soot because no equilibrium condition is maintained between the particle surface and the surrounding gas. These reasons would help to explain the soot disappearance in the heating treatment at the observed temperatures.

The decrease of A_{D4}/A_G in Fig. 6a indicates the decrease of defects such as non-hexagonal rings or vacancies within the polyaromatic units or cross-linkage between the polyaromatic units and carbon chains. Smaller values of the A_{D4}/A_G ratio also corresponds to a higher level of aromatisation and higher concentration of sp^2 hybridized carbon atoms [20] in the higher-heat-treated samples. This finding is consistent with the decrease of A_{D4}/A_G observed by Saffaripour et al. 2017 [38]. The defect and disorder reduction vs. heating temperature are also evidenced for OP6 and OP7 in Fig. 5, and Fig. 10 where full widths at half maximum of *D* and *G* peaks are narrower. In particular, while the *D* peak decreases approximately 120 cm^{-1}, the width of *G* peak diminishes about 15 - 20 cm^{-1}. The narrower of *D* and *G* peaks is due to the instability vs. the heat treatment of shoulder peaks such as D_4 and D'_1 and carbonyl groups indicated in Figs. 6 a, b, e.

Following our explanation in subsection 4.1, the vibration of C-H bonds of PAHs is considered as the origin of the *B* band in our spectra. We suspect that C-H "out-of-plane" bending modes originate from PAH consisting of mono-substituted groups and ortho-substitution of that PAH [97]. In Fig. 6 c, the B peak slightly decreases up to 200 °C and then rapidly drops and nearly disappears at 350 – 400 °C which confirms the removal of C-H bonds from the PAH. The aromatic C-H stretching bond is much stronger than other types of substitution which leads to their disappearance at higher temperature.

It is undeniable that OP6, OP7 soot highly contains matrix-bonded organics of various kinds; however, it is difficult to know whether all the detected organic species in our samples are actually internally included in the soot structure during its formation or are externally condensable, semi-volatile

molecular species emitted in the gas phase by the miniCAST and then stuck on the sapphire windows alongside the solid core particles. Most of organic compounds including PAH have their melting temperatures around few tens to approximately 200 ºC [98,99]. As a consequence of their independent existences in flame by-products, they are expected to transform around their melting points. Indeed, in Fig. 4, the photoluminescence signals start declining at 70 – 200 ºC and then at 350 – 400 ºC, both Raman and photoluminescence signals significantly decrease. The first observed declination could come from the transformation of condensed low / semi volatility organics coated / condensed on the particles [100]. The rather high evaporation / transformation temperature at around 350 – 400 ºC of the refractory organic carbon components indicates that they are incorporated into and part of the internal soot carbon nanostructures. These results are consistent with our previous studies using aerosol mass spectroscopy [21].

Thermal effect on polyaromatic units

Our HRTEM observations on untreated soot pointed out that the primary soot particles contain small geometric mean fringe lengths varying from 0.50 to 0.61 nm [21]. For such small fringe lengths, the *D* peak strength is proportional to the probability of finding a sixfold ring in the polyaromatic unit, that is corresponding to this unit area [45]. Hence, the polyaromatic unit mean size or the crystallite size L_a [Å] can be estimated by the Ferrari-Robertson relationship [45]:

$$\frac{\mathrm{I}_D}{\mathrm{I}_G} = \mathrm{C}'(\lambda) L_\mathrm{a}^2 \qquad (1)$$

where $\mathrm{I}_D/\mathrm{I}_G$ is the intensity ratio of *D* and *G* peaks which is proportional to the number and clustering of rings [45]. C'(λ) is excitation-wavelength-dependent and C'(532 nm) ≈ 0.0063 [45,101].

It is not established whether the $\mathrm{I}_D/\mathrm{I}_G$ ratio should be the ratio of the peak heights or peak areas [45]. In Fig. 7, whatever area ratio of *D* and *G* peaks or intensity ratio from non-fitted data or fitted data is used, the $\mathrm{I}_D/\mathrm{I}_G$ ratio is quadratic functions of the fringe length, L_{fringe}, of soot particles obtained by HRTEM, as expected from Eq. 1. However, the area and intensity ratios of the non-fitted *D* and *G*

peaks are strongly affected by D_1', D_4, ether and carbonyl bands originating from the OC, their ratios thus could not reflect only the polyaromatic unit of graphitic structures. As a result of the *D* peak being more affected by the OC than the *G* peak, the non-fitted peak ratios have been found to be higher than the fitted peak ratio. The intensity ratio of the fitted D_1 and *G* peaks is thus selected as a representative of I_D/I_G ratio avoiding the OC influences.

A correlation of the polyaromatic unit size, as deduced from Eq. 1, and fringe lengths is displayed in Fig. 8, where L_a is found to be twice as large as than the fringe lengths extracted from the HRTEM image analysis. This discrepancy may originate either from the applicability of Ferrari-Robertson relation which stated the proportionality of I_D/I_G to the number of ordered rings [19] or from the tortuosity/curvature of the fringe in HRTEM measurements [20]. Besides aromatic rings, our soot samples with high OC fraction (OP5-OP7) exhibit a contribution of olefinic chains that will be explained in Fig. 10. They thus conflict with the requirement of Ferrari-Robertson formula. In addition, due to potential bias, the fringe length was extracted from HRTEM could be shorter than a real length although three different HRTEM images of each samples were used to reduce the uncertainty.

Figure 9 shows different trends for soot exposed to the heating to elevated temperatures. In OP1 soot, the I_{D1}/I_G ratio is observed to be relatively constant in the whole temperature range indicating a negligible thermal effect on the structure. For the rich organic soot (OP5-7), two trends are observed with increasing temperature. First, a decline of the I_{D1}/I_G ratio can be observed from 25 ^oC up to a few hundred degrees. It may originate from the evaporation of the OC volatile component and cyclisation for increasing temperatures below 400°C which are also indicated by the narrower width of *G* peak in Fig. 10. Above 400 ^oC where the I_{D1}/I_G increases with increasing temperature, corresponds to the carbonization domain (removal of the heteroatom, here O and H) with concomitant formation of polyaromatic domain.

4.3. Evolution of the Raman band intensities

Raman band intensities for the different OPs

Under the same experimental conditions, the observed Raman signal *S* is affected by the scatterer density, the differential Raman cross section and the mass absorption coefficient [102–104]. Although no exact value could be determined, it is clear that the number of C atoms (the scatterers) at the same probe volume is lower for the higher OP because the miniCAST soot mass density decreases with increasing OC content [35]. On the one hand, the probe volume of the excitation laser becomes higher for higher OPs because the mass absorption coefficient decreases with the OC content. In Fig. 4, the observed Raman signals (S) of non heat-treated samples from OP1 to OP7 follows an upward trend with 1.25×10^7, 2.5×10^7, 5.0×10^7, and 8.0×10^7 count/s, respectively. We observed that the increase of Raman signal for higher OPs quantitatively follows the OC/TC content in the soot. However, densities and mass absorption coefficients differences could not explain the large variation and the increase is probably due to a modification of the Raman efficiency due to the OC. In particular, it could be the result of a "lensing effect" because of soot absorption enhancement due to internal mixing with / coated by other chemical species such as OC [105–108] or the presence of absorbing organic species either internally or externally mixed with the particles [105,109]. Additional work should be performed to investigate this carefully.

Heat treatment dependence

The heating process also influences the Raman band intensities of soot as seen with the changes of the observed Raman signal *S* in Fig. 4. While *S* of OP1 soot increases as a function of the temperature, that of OP5, 6 and 7 soot starts with a stable trend followed by an attenuation. The former may originate from the structural reorganisation of the sp^2 aromatic carbons with temperature increase since the Raman spectral contribution from OC in such sample is negligible. The latter is more probably a result of the competition between the reorganisation of the sp^2 phase and the evaporation/transformation of OC including PAHs during carbonization.

In Fig. 10, unlike non heat-treated OP1 soot whose G peak position is at 1600 cm^{-1}, the G peak

position of non heat-treated OP5-OP7 soot reaches values higher than 1600 cm^{-1}. This feature of OP1 soot is consistent with a material with only sp^2 rings and no olefinic chains [46] while that of OP5-OP7 soot indicates the olefinic chains contribution beside of the aromatic rings. When the heat treatment temperature increase, the *G* peak position of OP1 soot increases continuously while the FWHM has a rather constant value. This evolution is concomitant with the evolution of the band intensities (Fig. 4) which traces the carbonization process. For the other soot samples, the G band position is rather constant within the uncertainties. The relative increase of *G* band intensity together with its position in OP1 soot may trace formation of the olefinic chains caused by the heat treatment. However, additional studies, for instances exploring the band gap evolution, would be necessary to conclude on that.

Conclusions

This paper presents a spectral analysis of Raman and photoluminescence signals from various soot types produced by a mini-CAST soot generator, and also how these characteristic features changes as a result of heating in an inert nitrogen atmosphere. The study includes four different soot types from black aggregated soot with low organic fraction (OP1) to brownish smaller soot particles with high organic fraction (OP7). The main contributions from the present Raman spectroscopic study are:

- During heat treatment of the soot to elevated temperatures, we observe a strong decrease of the broadband photoluminescence as well as of the characteristic Raman peaks related to the organic compounds.
- The appearance of peaks related to C-H “out-of-plane” bending motions and sp hybridization showing thermal instability has been discussed for the first time for deposited soot. They clearly reveal in soot rich in OC and can be associated to species formed during the early soot formation processes.
- Contribution of ether and carbonyl oxygenated bonds could be detected, thereby providing a chemical speciation of the oxygenated groups in the organic compounds.

- Raman band intensity dependence on the OC content was discussed, and it was found to increase for the OP cases with higher OC content.

Our experiments were repeated many times producing the same results. The main uncertainty of this study comes from the data treatment, particularly the difficulty of photoluminescence subtraction on the rich OC soot (OP7). The uncertainty assessment of the photoluminescence subtraction in Raman spectral studies on "immature" / young / rich OC soot should be carried out in the future. Further work involving oxidation processes is required to better understand the reactivity of PAH and organic compounds in soot particles. In addition, a combination with other techniques such as infra-red and visible-UV spectroscopies for studying annealing effects is also necessary to better understand the transformation of OC in rich organic soot.

Acknowledgment

This work was supported by the European Union's Horizon 2020 research and innovation program under the Marie Skłodowska-Curie grant agreement [EU project 794156 – USFAOD] and the Swedish Research Council Formas [project 2018-00949].

References

[1] Z.A. Mansurov, Formation of soot from polycyclic aromatic hydrocarbons as well as fullerenes and carbon nanotubes in the combustion of hydrocarbon, J. Eng. Phys. Thermophys. 84 (2011) 125–159. doi:10.1007/s10891-011-0459-y.

[2] H. Wang, Formation of nascent soot and other condensed-phase materials in flames, Proc. Combust. Inst. 33 (2011) 41–67. doi:10.1016/j.proci.2010.09.009.

[3] M. Frenklach, Reaction mechanism of soot formation in flames, Phys. Chem. Chem. Phys. 4 (2002) 2028–2037. doi:10.1039/b110045a.

[4] M. Alfè, B. Apicella, J.N. Rouzaud, A. Tregrossi, A. Ciajolo, The effect of temperature on soot properties in premixed methane flames, Combust. Flame. 157 (2019) 1959–1965.

doi:10.1016/j.combustflame.2010.02.007.

[5] C. Russo, A. Ciajolo, Effect of the flame environment on soot nanostructure inferred by Raman spectroscopy at different excitation wavelengths, Combust. Flame. 162 (2015) 2431–2441. doi:10.1016/j.combustflame.2015.02.011.

[6] A. Lucotti, C.S. Casari, M. Tommasini, A. Li Bassi, D. Fazzi, V. Russo, M. Del Zoppo, C. Castiglioni, F. Cataldo, C.E. Bottani, G. Zerbi, sp Carbon chain interaction with silver nanoparticles probed by Surface Enhanced Raman Scattering, Chem. Phys. Lett. 478 (2009) 45–50. doi:10.1016/j.cplett.2009.06.030.

[7] M. Alfè, B. Apicella, R. Barbella, J.N. Rouzaud, A. Tregrossi, A. Ciajolo, Structure-property relationship in nanostructures of young and mature soot in premixed flames, Proc. Combust. Inst. 32 I (2009) 697–704. doi:10.1016/j.proci.2008.06.193.

[8] E.M. Adkins, J.H. Miller, Extinction measurements for optical band gap determination of soot in a series of nitrogen-diluted ethylene/air non-premixed flames., Phys. Chem. Chem. Phys. 17 (2015) 2686–95. doi:10.1039/c4cp04452e.

[9] R.L. Vander Wal, A.J. Tomasek, Soot nanostructure: Dependence upon synthesis conditions, Combust. Flame. 136 (2004) 129–140. doi:10.1016/j.combustflame.2003.09.008.

[10] H.A. Michelsen, Probing soot formation, chemical and physical evolution, and oxidation: A review of in situ diagnostic techniques and needs, Proc. Combust. Inst. 36 (2017) 717–735. doi:10.1016/j.proci.2016.08.027.

[11] G.M. Faeth, Köylü, Soot morphology and optical properties in nonpremixed turbulent flame environments, Combust. Sci. Technol. 108 (1995) 207–229. doi:10.1080/00102209508960399.

[12] I. Colbeck, B. Atkinson, Y. Johar, The morphology and optical properties of soot produced by different fuels, J. Aerosol Sci. 28 (1997) 715–723. doi:10.1016/S0021-8502(96)00466-1.

[13] A.D. Abid, J. Camacho, D.A. Sheen, H. Wang, Quantitative measurement of soot particle size distribution in premixed flames - The burner-stabilized stagnation flame approach, Combust. Flame. 156 (2009) 1862–1870. doi:10.1016/j.combustflame.2009.05.010.

[14] H. Bladh, N.-E. Olofsson, T. Mouton, J. Simonsson, X. Mercier, A. Faccinetto, P.-E. Bengtsson, P. Desgroux, Probing the smallest soot particles in low-sooting premixed flames using laser-induced incandescence, Proc. Combust. Inst. 35 (2015) 1843–1850. doi:10.1016/j.proci.2014.06.001.

[15] A. Ciajolo, Condensed phases in soot formation process, in: H. Bockhorn, A. D'Anna, A.F. Sarofim, H. Wang (Eds.), Combust. Gener. Fine Carbonaceous Part., KIT scientific publishing, Karlsruhe, 2009: pp. 333–344.

[16] M.L. Botero, N. Eaves, J.A.H. Dreyer, Y. Sheng, J. Akroyd, W. Yang, M. Kraft, Experimental and numerical study of the evolution of soot primary particles in a diffusion flame, Proc. Combust. Inst. 37 (2019) 2047–2055. doi:10.1016/j.proci.2018.06.185.

[17] M.L. Botero, Y. Sheng, J. Akroyd, J. Martin, J.A.H. Dreyer, W. Yang, M. Kraft, Internal structure of soot particles in a diffusion flame, Carbon N. Y. 141 (2019) 635–642. doi:10.1016/j.carbon.2018.09.063.

[18] H.F. Calcote, Mechanisms of soot nucleation in flames-A critical review, Combust. Flame. 42 (1981) 215–242. doi:10.1016/0010-2180(81)90159-0.

[19] E. Cenker, W.L. Roberts, Quantitative effects of rapid heating on soot-particle sizing through analysis of two-pulse LII, Appl. Phys. B Lasers Opt. 123 (2017) 1–10. doi:10.1007/s00340-017-6653-7.

[20] R. Dastanpour, A. Momenimovahed, K. Thomson, J. Olfert, S. Rogak, Variation of the optical properties of soot as a function of particle mass, Carbon N. Y. 124 (2017) 201–211. doi:10.1016/j.carbon.2017.07.005.

[21] V.B. Malmborg, A.C. Eriksson, S. Török, Y. Zhang, K. Kling, J. Martinsson, E.C. Fortner, L. Gren, S. Kook, T.B. Onasch, P.-E. Bengtsson, J. Pagels, Relating aerosol mass spectra to composition and nanostructure of soot particles, Carbon N. Y. 142 (2019) 535–546. doi:10.1016/j.carbon.2018.10.072.

[22] B. Apicella, P. Pré, M. Alfè, A. Ciajolo, V. Gargiulo, C. Russo, A. Tregrossi, D. Deldique, J.N. Rouzaud, Soot nanostructure evolution in premixed flames by High Resolution Electron Transmission Microscopy (HRTEM), Proc. Combust. Inst. 35 (2015) 1895–1902. doi:10.1016/j.proci.2014.06.121.

[23] B. Apicella, A. Ciajolo, A. Tregrossi, J. Abrahamson, R.L. Vander Wal, C. Russo, HRTEM and EELS investigations of flame-formed soot nanostructure, Fuel. 225 (2018). doi:10.1016/j.fuel.2018.03.091.

[24] S.H. Park, M.Y. Choi, A. Yozgatligil, Nanostructure of soot collected from ethanol droplet flames in microgravity, Combust. Sci. Technol. 181 (2009) 1164–1186. doi:10.1080/00102200903074154.

[25] P. Desgroux, X. Mercier, K.A. Thomson, Study of the formation of soot and its precursors in flames using optical diagnostics, Proc. Combust. Inst. 34 (2013) 1713–1738. doi:10.1016/j.proci.2012.09.004.

[26] J. Yon, E. Therssen, F. Liu, S. Bejaoui, D. Hebert, Influence of soot aggregate size and internal multiple scattering on LII signal and the absorption function variation with wavelength determined by the TEW-LII method, Appl. Phys. B Lasers Opt. 119 (2015) 643–655. doi:10.1007/s00340-015-6116-y.

[27] K.O. Johansson, F. El Gabaly, P.E. Schrader, M.F. Campbell, H.A. Michelsen, Evolution of maturity levels of the particle surface and bulk during soot growth and oxidation in a flame, Aerosol Sci. Technol. 51 (2017) 1333–1344. doi:10.1080/02786826.2017.1355047.

[28] J. Camacho, Y. Tao, H. Wang, Kinetics of nascent soot oxidation by molecular oxygen in a flow reactor, Proc. Combust. Inst. 35 (2015) 1887–1894. doi:10.1016/j.proci.2014.05.095.

[29] P. Toth, D. Jacobsson, M. Ek, H. Wiinikka, Real-time, in situ, atomic scale observation of soot oxidation, Carbon N. Y. 145 (2019) 149–160. doi:10.1016/j.carbon.2019.01.007.

[30] P.R. Buseck, K. Adachi, A. Gelencsér, É. Tompa, M. Pósfai, Ns-Soot: A Material-Based Term for Strongly Light-Absorbing Carbonaceous Particles, Aerosol Sci. Technol. 48 (2014) 777–788. doi:10.1080/02786826.2014.919374.

[31] H. Bockhorn, A. D'Anna, A.F. Sarofim, H. Wang, Combustion generated fine carbonaceous particles, KIT scientific publishing, Karlsruhe, 2007. doi:10.5445/KSP/1000013744.

[32] A. Faccinetto, C. Focsa, P. Desgroux, M. Ziskind, Progress toward the Quantitative Analysis of PAHs Adsorbed on Soot by Laser Desorption/Laser Ionization/Time-of-Flight Mass Spectrometry, Environ. Sci. Technol. 49 (2015) 10510–10520. doi:10.1021/acs.est.5b02703.

[33] P. Parent, C. Laffon, I. Marhaba, D. Ferry, T.Z. Regier, I.K. Ortega, B. Chazallon, Y. Carpentier, C. Focsa, Nanoscale characterization of aircraft soot: A high-resolution transmission electron microscopy, Raman spectroscopy, X-ray photoelectron and near-edge X-ray absorption spectroscopy study, Carbon N. Y. 101 (2016) 86–100. doi:10.1016/j.carbon.2016.01.040.

[34] S. Török, V.B. Malmborg, J. Simonsson, A. Eriksson, J. Martinsson, M. Mannazhi, J. Pagels, P.E. Bengtsson, Investigation of the absorption Ångström exponent and its relation to physicochemical properties for mini-CAST soot, Aerosol Sci. Technol. 52 (2018) 757–767. doi:10.1080/02786826.2018.1457767.

[35] J. Yon, A. Bescond, F.X. Ouf, A simple semi-empirical model for effective density measurements of fractal aggregates, J. Aerosol Sci. 87 (2015) 28–37. doi:10.1016/j.jaerosci.2015.05.003.

[36] L. Mueller, G. Jakobi, J. Orasche, E. Karg, M. Sklorz, G. Abbaszade, B. Weggler, L. Jing, J. Schnelle-Kreis, R. Zimmermann, Online determination of polycyclic aromatic hydrocarbon formation from a flame soot generator Aerosols and Health, Anal. Bioanal. Chem. 407 (2015) 5911–5922. doi:10.1007/s00216-015-8549-x.

[37] M.N. Ess, D. Ferry, E.D. Kireeva, R. Niessner, F.X. Ouf, N.P. Ivleva, In situ Raman microspectroscopic analysis of soot samples with different organic carbon content: Structural changes during heating, Carbon N. Y. 105 (2016) 572–585. doi:10.1016/j.carbon.2016.04.056.

[38] M. Saffaripour, L.L. Tay, K.A. Thomson, G.J. Smallwood, B.T. Brem, L. Durdina, M. Johnson, Raman spectroscopy and TEM characterization of solid particulate matter emitted from soot generators and aircraft turbine engines, Aerosol Sci. Technol. 51 (2017) 518–531. doi:10.1080/02786826.2016.1274368.

[39] M.M. Maricq, Examining the relationship between black carbon and soot in flames and engine exhaust, Aerosol Sci. Technol. 48 (2014) 620–629. doi:10.1080/02786826.2014.904961.

[40] T.C. Bond, R.W. Bergstrom, Light Absorption by Carbonaceous Particles: An Investigative Review, Aerosol Sci. Technol. 40 (2006) 27–67. doi:10.1080/02786820500421521.

[41] A. Mamakos, I. Khalek, R. Giannelli, M. Spears, Characterization of combustion aerosol produced by a mini-CAST and treated in a catalytic stripper, Aerosol Sci. Technol. 47 (2013) 927–936. doi:10.1080/02786826.2013.802762.

[42] R.H. Moore, L.D. Ziemba, D. Dutcher, A.J. Beyersdorf, K. Chan, S. Crumeyrolle, T.M. Raymond, K.L. Thornhill, E.L. Winstead, B.E. Anderson, Mapping the operation of the miniature combustion aerosol standard (Mini-CAST) soot generator, Aerosol Sci. Technol. 48 (2014) 467–479. doi:10.1080/02786826.2014.890694.

[43] F. Tuinstra, J.L. Koenig, Raman Spectrum of Graphite, J. Chem. Phys. 53 (1970) 1126. doi:10.1063/1.1674108.

[44] M. Dresselhaus, Light Scattering in Graphite Intercalation Compounds, Light Scatt. Solids III. 20 (1982) 3–57. doi:10.1007/3540115137_2.

[45] A. Ferrari, J. Robertson, Interpretation of Raman spectra of disordered and amorphous carbon, Phys. Rev. B. 61 (2000) 14095–14107. doi:10.1103/PhysRevB.61.14095.

[46] A.C. Ferrari, J. Robertson, Resonant Raman spectroscopy of disordered, amorphous, and diamondlike carbon, Phys. Rev. B. 64 (2001) 075414. doi:10.1103/PhysRevB.64.075414.

[47] M.A. Pimenta, G. Dresselhaus, M.S. Dresselhaus, L.G. Cançado, A. Jorio, R. Saito, Studying disorder in graphite-based systems by Raman spectroscopy, Phys. Chem. Chem. Phys. 9 (2007) 1276–1291. doi:10.1039/b613962k.

[48] Y. Wang, D.C. Alsmeyer, R.L. McCreery, Raman Spectroscopy of Carbon Materials: Structural Basis of Observed Spectra, Chem. Mater. 2 (1990) 557–563. doi:10.1021/cm00011a018.

[49] A. Oberlin, M. Villey, A. Combaz, Influence of elemental composition on carbonization, Carbon N. Y. 18 (1980) 347–353. doi:10.1016/0008-6223(80)90006-8.

[50] C. Jäger, T. Henning, R. Schlögl, O. Spillecke, Spectral properties of carbon black, J. Non. Cryst. Solids. 258 (1999) 161–179. doi:10.1016/S0022-3093(99)00436-6.

[51] A. Sadezky, H. Muckenhuber, H. Grothe, R. Niessner, U. Pöschl, Raman microspectroscopy of soot and related carbonaceous materials: Spectral analysis and structural information, Carbon N. Y. 43 (2005) 1731–1742. doi:10.1016/j.carbon.2005.02.018.

[52] S. Reich, C. Thomsen, Raman spectroscopy of graphite, Philos. Trans. R. Soc. A Math. Phys. Eng. Sci. 362 (2004) 2271–2288. doi:10.1098/rsta.2004.1454.

[53] A. Cuesta, P. Dhamelincourt, J. Laureyns, A. Martínez-Alonso, J.M.D. Tascón, Raman microprobe studies on carbon materials, Carbon N. Y. 32 (1994) 1523–1532. doi:10.1016/0008-6223(94)90148-1.

[54] M. Pawlyta, J.-N. Rouzaud, S. Duber, Raman microspectroscopy characterization of carbon blacks: Spectral analysis and structural information, Carbon N. Y. 84 (2015) 479–490. doi:10.1016/j.carbon.2014.12.030.

[55] Y. Carpentier, G. Féraud, E. Dartois, R. Brunetto, E. Charon, A.-T. Cao, L. d'Hendecourt, P. Bréchignac, J.-N. Rouzaud, T. Pino, Nanostructuration of carbonaceous dust as seen through the positions of the 6.2 and 7.7 μ m AIBs, Astron. Astrophys. 548 (2012) A40. doi:10.1051/0004-6361/201118700.

[56] W.S. Bacsa, J.S. Lannin, D.L. Pappas, J.J. Cuomo, Raman scattering of laser-deposited amorphous carbon, Phys. Rev. B. 47 (1993) 10931–10934. doi:10.1103/PhysRevB.47.10931.

[57] T. LópezRíos, É. Sandré, S. Leclercq, É. Sauvain, Polyacetylene in diamond films evidenced by surface enhanced Raman scattering, Phys. Rev. Lett. 76 (1996) 4935–4938. doi:10.1103/PhysRevLett.76.4935.

[58] B. Dippel, H. Jander, J. Heintzenberg, NIR FT Raman spectroscopic study of flame soot, Phys. Chem. Chem. Phys. 1 (1999) 4707–4712. doi:10.1039/a904529e.

[59] H.J. Seong, A.L. Boehman, Evaluation of Raman parameters using visible Raman microscopy for soot oxidative reactivity, Energy and Fuels. 27 (2013) 1613–1624. doi:10.1021/ef301520y.

[60] P. Mallet-Ladeira, P. Puech, P. Weisbecker, G.L. Vignoles, M. Monthioux, Behavior of Raman D band for pyrocarbons with crystallite size in the 2-5 nm range, Appl. Phys. A Mater. Sci. Process. 114 (2014) 759–763. doi:10.1007/s00339-013-7671-x.

[61] P. Mallet-Ladeira, P. Puech, C. Toulouse, M. Cazayous, N. Ratel-Ramond, P. Weisbecker,

G.L. Vignoles, M. Monthioux, A Raman study to obtain crystallite size of carbon materials: A better alternative to the Tuinstra-Koenig law, Carbon N. Y. 80 (2014) 629–639. doi:10.1016/j.carbon.2014.09.006.

[62] P. Puech, J.M. Plewa, P. Mallet-Ladeira, M. Monthioux, Spatial confinement model applied to phonons in disordered graphene-based carbons, Carbon N. Y. 105 (2016) 275–281. doi:10.1016/j.carbon.2016.04.048.

[63] J. Ribeiro-Soares, M.E. Oliveros, C. Garin, M. V. David, L.G.P. Martins, C.A. Almeida, E.H. Martins-Ferreira, K. Takai, T. Enoki, R. Magalhães-Paniago, A. Malachias, A. Jorio, B.S. Archanjo, C.A. Achete, L.G. Cançado, Structural analysis of polycrystalline graphene systems by Raman spectroscopy, Carbon N. Y. 95 (2015) 646–652. doi:10.1016/j.carbon.2015.08.020.

[64] Y. Liu, C. Liu, J. Ma, Q. Ma, H. He, Structural and hygroscopic changes of soot during heterogeneous reaction with O3, Phys. Chem. Chem. Phys. 12 (2010) 10896–10903. doi:10.1039/c0cp00402b.

[65] Y. Carpentier, T. Pino, P. Bréchignac, R2PI spectroscopy of aromatic molecules produced in an ethylene-rich flame, J. Phys. Chem. A. 117 (2013) 10092–10104. doi:10.1021/jp400913n.

[66] F. Negri, C. Castiglioni, M. Tommasini, G. Zerbi, A computational study of the Raman spectra of large polycyclic aromatic hydrocarbons: Toward molecularly defined subunits of graphite, J. Phys. Chem. A. 106 (2002) 3306–3317. doi:10.1021/jp0128473.

[67] K.-C. Le, C. Lefumeux, P.-E. Bengtsson, T. Pino, Direct observation of aliphatic structures in soot particles produced in low-pressure premixed ethylene flames via online Raman spectroscopy, Proc. Combust. Inst. 37 (2019) 869–876. doi:10.1016/j.proci.2018.08.003.

[68] P.G. Li, M. Lei, W.H. Tang, Raman and photoluminescence properties of α-Al2O3microcones with hierarchical and repetitive superstructure, Mater. Lett. 64 (2010)

161–163. doi:10.1016/j.matlet.2009.10.032.

[69] G.A. Zickler, B. Smarsly, N. Gierlinger, H. Peterlik, O. Paris, A reconsideration of the relationship between the crystallite size La of carbons determined by X-ray diffraction and Raman spectroscopy, Carbon N. Y. 44 (2006) 3239–3246. doi:10.1016/j.carbon.2006.06.029.

[70] N. Larouche, B.L. Stansfield, Classifying nanostructured carbons using graphitic indices derived from Raman spectra, Carbon N. Y. 48 (2010) 620–629. doi:10.1016/j.carbon.2009.10.002.

[71] S. Bejaoui, X. Mercier, P. Desgroux, E. Therssen, Laser induced fluorescence spectroscopy of aromatic species produced in atmospheric sooting flames using UV and visible excitation wavelengths, Combust. Flame. 161 (2014) 2479–2491. doi:10.1016/j.combustflame.2014.03.014.

[72] C. Pardanaud, C. Martin, G. Giacometti, P. Roubin, B. Pégourié, C. Hopf, T. Schwarz-Selinger, W. Jacob, J.G. Buijnsters, Long-term H-release of hard and intermediate between hard and soft amorphous carbon evidenced by in situ Raman microscopy under isothermal heating, Diam. Relat. Mater. 37 (2013) 92–96. doi:10.1016/j.diamond.2013.05.001.

[73] C. Pardanaud, C. Martin, P. Roubin, G. Giacometti, C. Hopf, T. Schwarz-Selinger, W. Jacob, Raman spectroscopy investigation of the H content of heated hard amorphous carbon layers, Diam. Relat. Mater. 34 (2013) 100–104. doi:10.1016/j.diamond.2013.02.009.

[74] B.S. Haynes, H.G. Wagner, Soot formation, Prog. Energy Combust. Sci. 7 (1981) 229–273. doi:10.1016/0360-1285(81)90001-0.

[75] A. Ciajolo, R. Ragucci, B. Apicella, R. Barbella, M. De Joannon, A. Tregrossi, Fluorescence spectroscopy of aromatic species produced in rich premixed ethylene flames, Chemosphere. 42 (2001) 835–841. doi:10.1016/S0045-6535(00)00258-7.

[76] Y. Zhang, Y. Li, L. Wang, P. Liu, R. Zhan, Z. Huang, H. Lin, Investigation on the LIF

spectrum superposition of gas-phase PAH mixtures at elevated temperatures: potential for the analysis of PAH LIF spectra in sooting flames, Appl. Phys. B Lasers Opt. 125 (2019). doi:10.1007/s00340-019-7185-0.

[77] Y. Kawashima, G. Katagiri, Observation of the out-of-plane mode in the raman scattering from the graphite edge plane, Phys. Rev. B - Condens. Matter Mater. Phys. 59 (1999) 62–64. doi:10.1103/PhysRevB.59.62.

[78] C. Pardanaud, C. Martin, G. Cartry, A. Ahmad, L. Schiesko, G. Giacometti, M. Carrerea, P. Roubin, In-plane and out-of-plane defects of graphite bombarded by H, D and He investigated by atomic force and Raman microscopies, J. Raman Spectrosc. 46 (2015) 256–265. doi:10.1002/jrs.4624.

[79] A. Pathak, S. Rastogi, Computational study of neutral and cationic catacondensed polycyclic aromatic hydrocarbons, Chem. Phys. 313 (2005) 133–150. doi:10.1016/j.chemphys.2005.01.007.

[80] W.G.F. Daimay Lin-Vien, Norman B. Colthup, Jeanette Grasselli Brown, The Handbook of Infrared and Raman Characteristic Frequencies of Organic Molecules, 1st ed., 1991.

[81] F. Innocenti, A. Milani, C. Castiglioni, Can Raman spectroscopy detect cumulenic structures of linear carbon chains?, J. Raman Spectrosc. 41 (2010) 226–236. doi:10.1002/jrs.2413.

[82] L. Shi, P. Rohringer, K. Suenaga, Y. Niimi, J. Kotakoski, J.C. Meyer, H. Peterlik, M. Wanko, S. Cahangirov, A. Rubio, Z.J. Lapin, L. Novotny, P. Ayala, T. Pichler, Confined linear carbon chains as a route to bulk carbyne, Nat. Mater. 15 (2016) 634–639. doi:10.1038/nmat4617.

[83] F. Cataldo, The role of Raman spectroscopy in the research on sp-hybridized carbon chains: Carbynoid structures polyynes and metal polyynides, J. Raman Spectrosc. 39 (2008) 169–176. doi:10.1002/jrs.1830.

[84] M. Kertész, J. Koller, A. Ažman, Ab initio Hartree-Fock crystal orbital studies. Energy bands in polyene reconsidered, J. Chem. Phys. 67 (1977) 1180–1186. doi:10.1063/1.434972.

[85] L. Ravagnan, P. Piseri, M. Bruzzi, S. Miglio, G. Bongiorno, A. Baserga, C.S. Casari, A. Li Bassi, C. Lenardi, Y. Yamaguchi, T. Wakabayashi, C.E. Bottani, P. Milani, Influence of cumulenic chains on the vibrational and electronic properties of sp-sp2 amorphous carbon, Phys. Rev. Lett. 98 (2007) 25–28. doi:10.1103/PhysRevLett.98.216103.

[86] L. Ravagnan, F. Siviero, C. Lenardi, P. Piseri, E. Barborini, P. Milani, C.S. Casari, A. Li Bassi, C.E. Bottani, Cluster-Beam Deposition and in situ Characterization of Carbyne-Rich Carbon Films, Phys. Rev. Lett. 89 (2002) 285506. doi:10.1103/PhysRevLett.89.285506.

[87] L. Kavan, Carbyne forms of Raman shift, Carbon N. Y. 32 (1994) 1533–1536.

[88] B. Apicella, O. Senneca, C. Russo, S. Heuer, L. Cortese, F. Cerciello, V. Scherer, M. Schiemann, A. Ciajolo, Separation and characterization of carbonaceous particulate (soot and char) produced from fast pyrolysis of coal in inert and CO2 atmospheres, Fuel. 201 (2017) 118–123. doi:10.1016/j.fuel.2016.11.049.

[89] R. Brunetto, T. Pino, E. Dartois, A.T. Cao, L. D'Hendecourt, G. Strazzulla, P. Bréchignac, Comparison of the Raman spectra of ion irradiated soot and collected extraterrestrial carbon, Icarus. 200 (2009) 323–337. doi:10.1016/j.icarus.2008.11.004.

[90] K.O. Johansson, T. Dillstrom, M. Monti, F. El Gabaly, M.F. Campbell, P.E. Schrader, D.M. Popolan-Vaida, N.K. Richards-Henderson, K.R. Wilson, A. Violi, H.A. Michelsen, Formation and emission of large furans and oxygenated hydrocarbons from flames, Proc. Natl. Acad. Sci. 113 (2016) 8374–8379. doi:10.1073/pnas.1604772113.

[91] J.L. Figueiredo, M.F.R. Pereira, M.M.A. Freitas, J.J.M. Órfão, Characterization of active sites on carbon catalysts, Ind. Eng. Chem. Res. 46 (2007) 4110–4115. doi:10.1021/ie061071v.

[92] F. Negri, E. Di Donato, M. Tommasini, C. Castiglioni, G. Zerbi, K. M??llen, Resonance Raman contribution to the D band of carbon materials: Modeling defects with quantum chemistry, J. Chem. Phys. 120 (2004) 11889–11900. doi:10.1063/1.1710853.

[93] A.C. Ferrari, S.E. Rodil, J. Robertson, S.E. Rodil, J. Robertson, Interpretation of infrared and Raman spectra of amorphous carbon nitrides, Phys. Rev. B - Condens. Matter Mater. Phys. 67 (2003) 1–20. doi:10.1103/PhysRevB.67.155306.

[94] T. Jawhari, A. Roid, J. Casado, Raman spectroscopic characterization of some commercially available carbon black materials, Carbon N. Y. 33 (1995) 1561–1565. doi:10.1016/0008-6223(95)00117-V.

[95] N.M.J. Conway, A.C. Ferrari, A.J. Flewitt, J. Robertson, W.I. Milne, A. Tagliaferro, W. Beyer, Defect and disorder reduction by annealing in hydrogenated tetrahedral amorphous carbon, Diam. Relat. Mater. 9 (2000) 765–770. doi:10.1016/S0925-9635(99)00271-X.

[96] G. Matuschek, E. Karg, A. Schröppel, H. Schulz, O. Schmid, Chemical investigation of eight different types of carbonaceous particles using thermoanalytical techniques, Environ. Sci. Technol. 41 (2007) 8406–8411. doi:10.1021/es062660v.

[97] A. Kumar, A.P. Singh, S. Kumari, P.K. Dutta, S.K. Dhawan, A. Dhar, Polyaromatic-hydrocarbon-based carbon copper composites for the suppression of electromagnetic pollution, J. Mater. Chem. A. 2 (2014) 16632–16639. doi:10.1039/c4ta01655f.

[98] N. 92 IARC working Group on the valuation of Carcinogenic Risks to Human, Some Non-heterocyclic Polycyclic Aromatic Hydrocarbon and Some Related Exposures, International Agency for Research on Cancer, Lyon, 2010. https://www.ncbi.nlm.nih.gov/books/NBK321712/.

[99] J.G.E. Phillips, National Physical Laboratory, (n.d.). doi:http://www.kayelaby.npl.co.uk/chemistry/3_3/3_3.html#P.

[100] R. Saleh, E.S. Robinson, D.S. Tkacik, A.T. Ahern, S. Liu, A.C. Aiken, R.C. Sullivan, A.A. Presto, M.K. Dubey, R.J. Yokelson, N.M. Donahue, A.L. Robinson, Brownness of organics in aerosols from biomass burning linked to their black carbon content, Nat. Geosci. 7 (2014) 647–650. doi:10.1038/ngeo2220.

[101] A.C. Ferrari, D.M. Basko, Raman spectroscopy as a versatile tool for studying the properties of graphene, Nat Nanotechnol. 8 (2013) 235–246. doi:10.1038/nnano.2013.46.

[102] M. Fryling, J.C. Frank, L.R. Mccreery, Intensity calibration and sensitivity comparisons for CCD/Raman spectrometers, Appl. Spectrosc. 47 (1993) 1965–1974.

[103] R.L. Mccreery, Photometric Standards for Raman Spectroscopy, John Wiley& Sons, Ltd, 2006. doi:10.1002/9780470027325.s0706.

[104] K.C. Le, C. Lefumeux, T. Pino, Differential Raman backscattering cross sections of black carbon nanoparticles, Sci. Rep. 7 (2017) 17124. doi:10.1038/s41598-017-17300-6.

[105] Y. Zhang, O. Favez, F. Canonaco, D. Liu, G. Močnik, T. Amodeo, J. Sciare, A.S.H. Prévôt, V. Gros, A. Albinet, Evidence of major secondary organic aerosol contribution to lensing effect black carbon absorption enhancement, Npj Clim. Atmos. Sci. 1 (2018). doi:10.1038/s41612-018-0056-2.

[106] C.D. Cappa, T.B. Onasch, P. Massoli, D.R. Worsnop, T.S. Bates, E.S. Cross, P. Davidovits, J. Hakala, K. Hayden, B.T. Jobson, K.R. Kolesar, D.A. Lack, B.M. Lerner, S.-M. Li, D. Mellon, I. Nuaaman, J. Olfert, T. Petäjä, P.K. Quinn, C. Song, R. Subramanian, A. Vlasenko, E.J. Williams, R.A. Zaver, On the magnitude of absorption enhancements due to mixing state of atmospheric black carbon, Science (80-.). (2012) submitted.

[107] S. Liu, A.C. Aiken, K. Gorkowski, M.K. Dubey, C.D. Cappa, L.R. Williams, S.C. Herndon, P. Massoli, E.C. Fortner, P.S. Chhabra, W.A. Brooks, T.B. Onasch, J.T. Jayne, D.R. Worsnop, S. China, N. Sharma, C. Mazzoleni, L. Xu, N.L. Ng, D. Liu, J.D. Allan, J.D. Lee,

Z.L. Fleming, C. Mohr, P. Zotter, S. Szidat, A.S.H. Prévôt, Enhanced light absorption by mixed source black and brown carbon particles in UK winter, Nat. Commun. 6 (2015). doi:10.1038/ncomms9435.

[108] D. Liu, J. Whitehead, M.R. Alfarra, E. Reyes-Villegas, D. V. Spracklen, C.L. Reddington, S. Kong, P.I. Williams, Y.C. Ting, S. Haslett, J.W. Taylor, M.J. Flynn, W.T. Morgan, G. McFiggans, H. Coe, J.D. Allan, Black-carbon absorption enhancement in the atmosphere determined by particle mixing state, Nat. Geosci. 10 (2017) 184–188. doi:10.1038/ngeo2901.

[109] M.O. Andreae, A. Gelencsér, Black carbon or brown carbon? The nature of light-absorbing carbonaceous aerosols, Atmos. Chem. Phys. 6 (2006) 3131–3148. doi:10.5194/acpd-6-3419-2006.

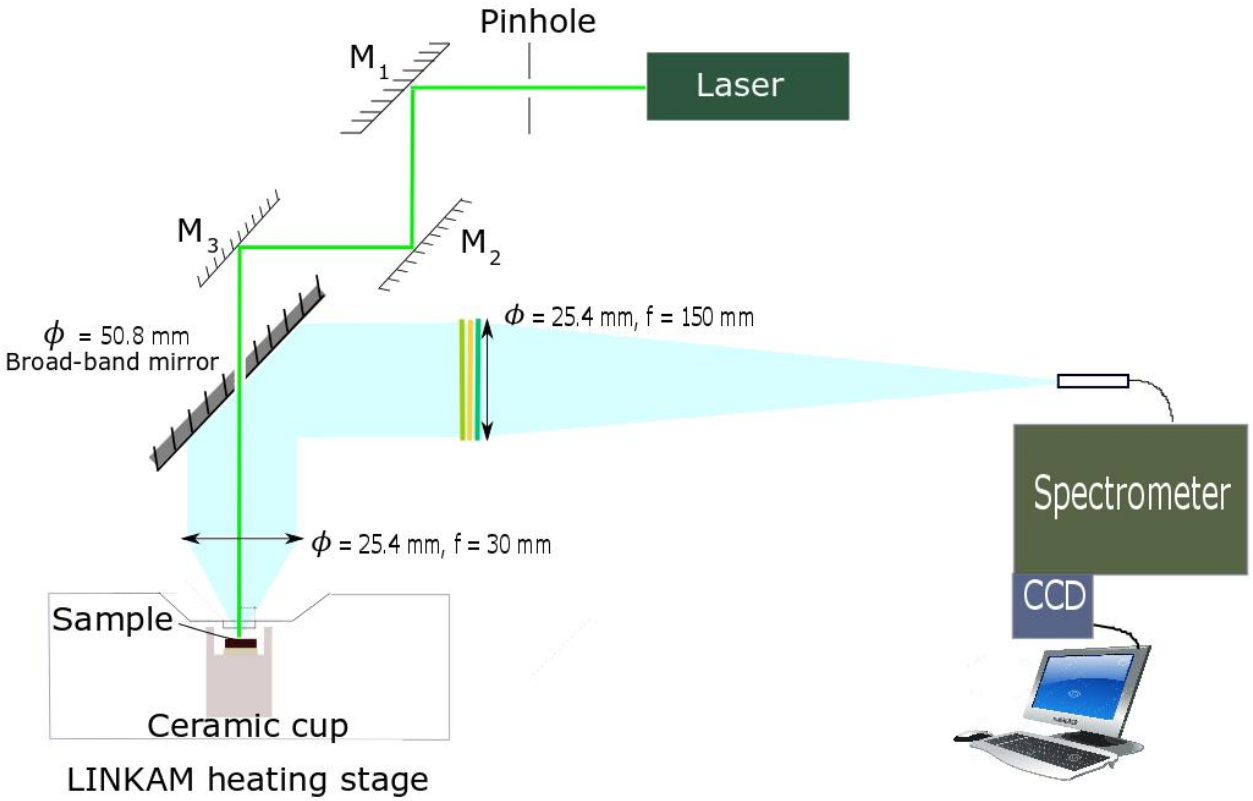

Fig. 1: Scheme of the home-built Raman experimental setup. Φ is diameter, f is focal length.

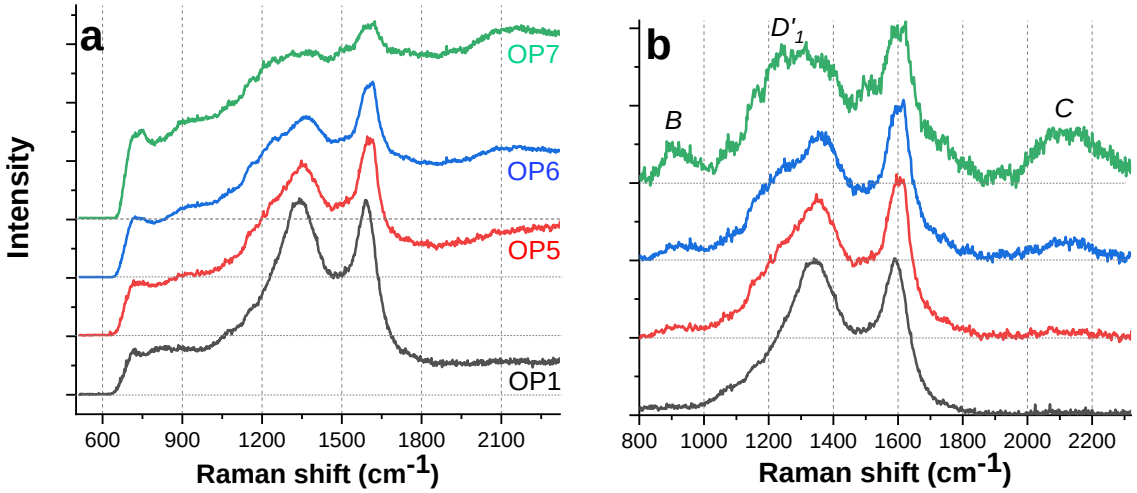

Fig. 2: Spectra of non-heat-treated OP1, OP5, OP6 and OP7 soot in N_2 environment before (a) and after (b) photoluminescence subtraction. Spectra are shifted vertically for clarity. Horizontal dash-lines show the zero level of each spectrum.

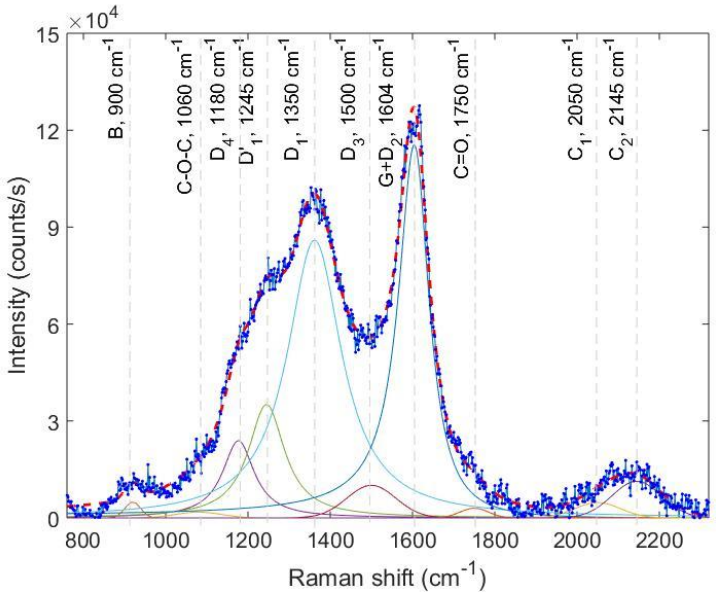

Fig. 3: Raman spectral deconvolutions of non-heat treated OP6 soot.

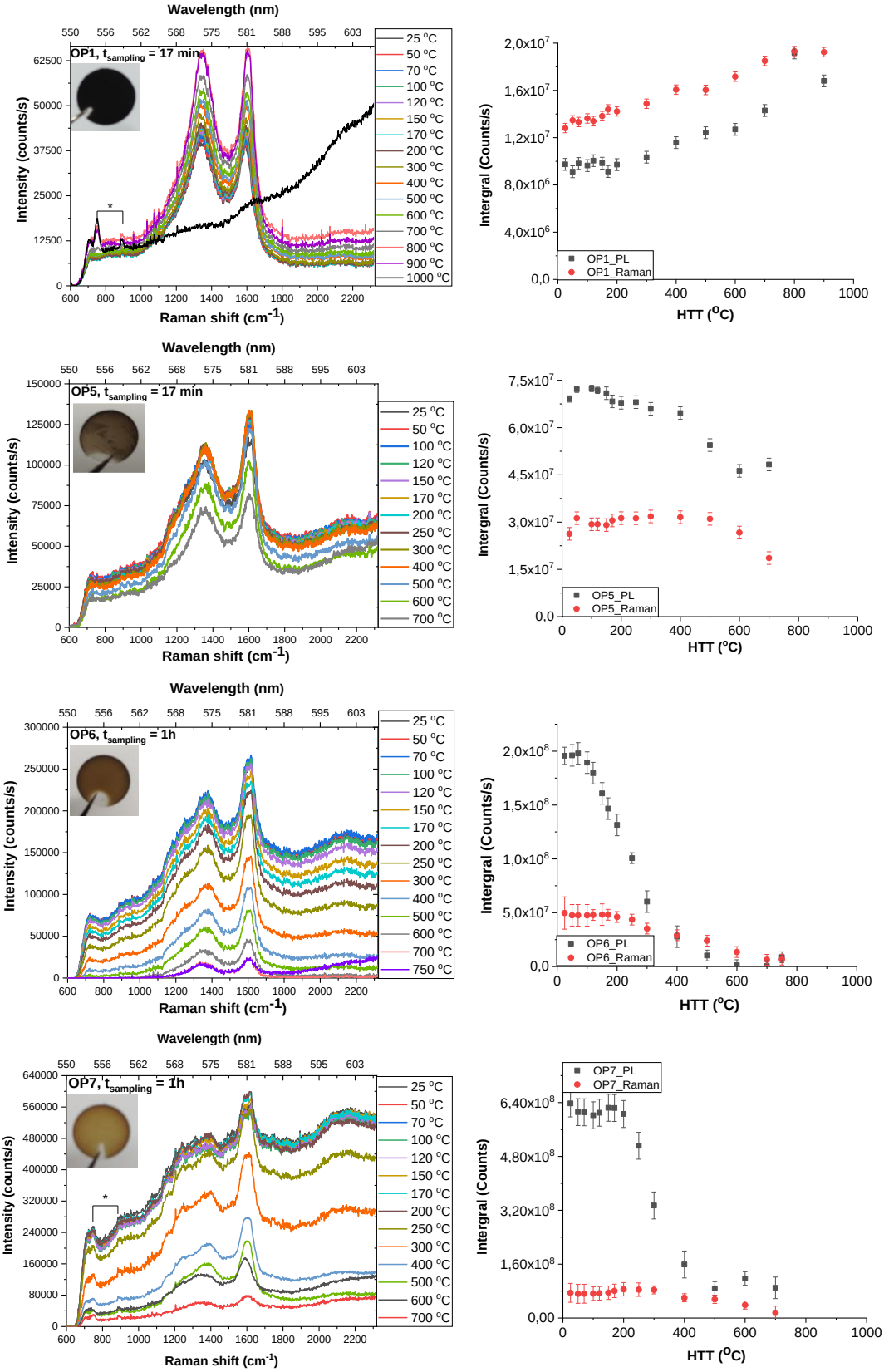

*Fig. 4: Spectral evolution (the 1st column) and observed Raman and photoluminescence (PL) signals (the 2nd column) of OP1, OP5, OP6 and OP7 soot samples vs. heat treatment temperature (HTT) in N_2 environment. *peaks arise from the sapphire substrate because of the lower covering of the sapphire plate.*

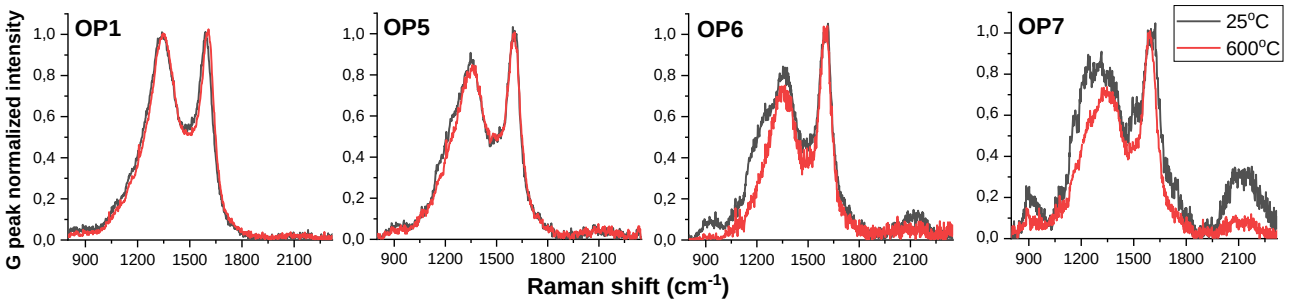

Fig. 5: G peak normalized Raman spectra of OP1, OP5, OP6, and OP7 at 25 °C and at 600 °C.

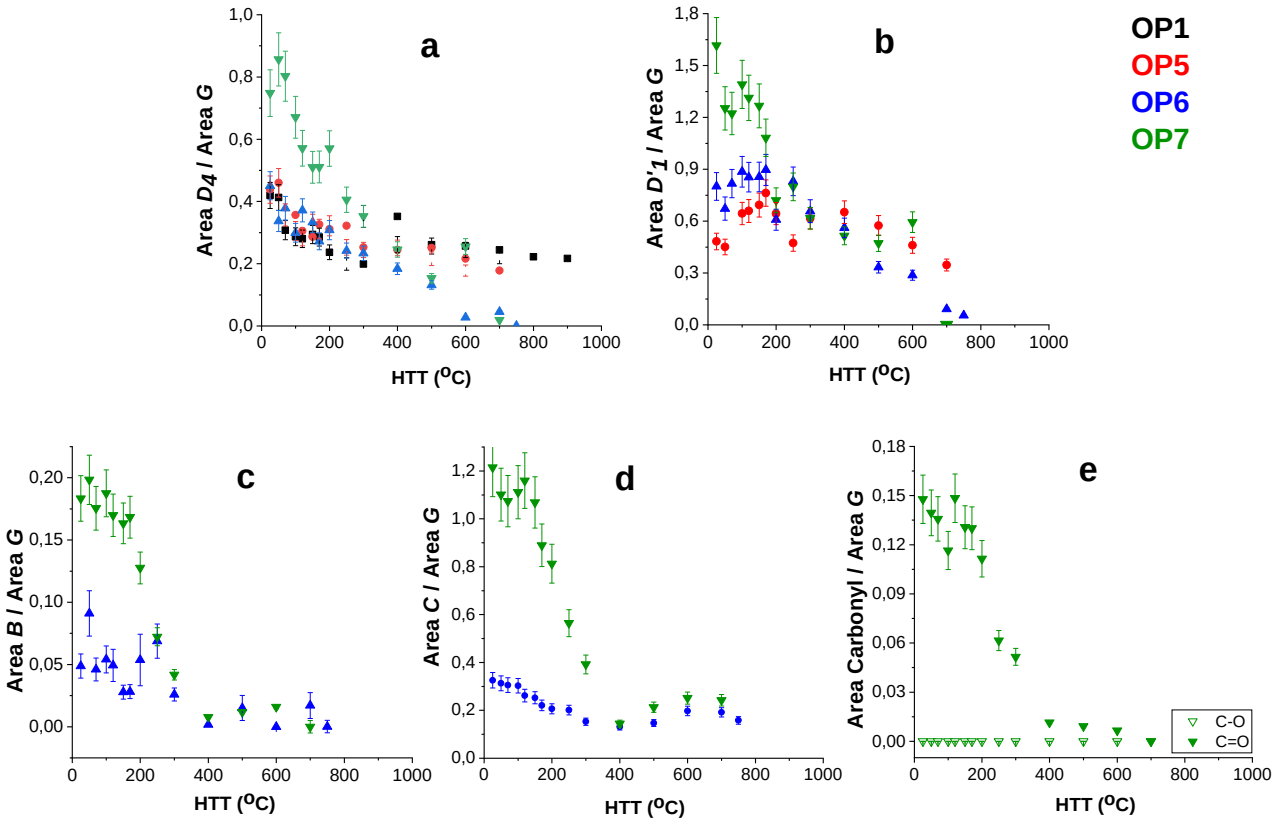

Fig. 6: The evolution of D_4 (a), D'_1 (b), B (c), sp (d), ether and carbonyl bonds (d) vs. heat treatment temperature (HTT).

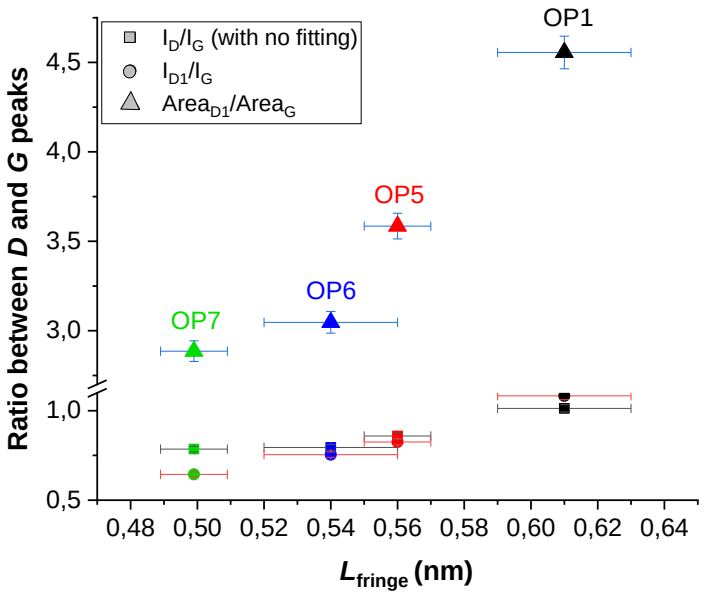

Fig. 7: Correlation of Height and Area ratios of D and G peaks in Raman spectra with the fringe lengths obtained by HRTEM [21] *of non heat-treated soot. I indicates peak intensity.*

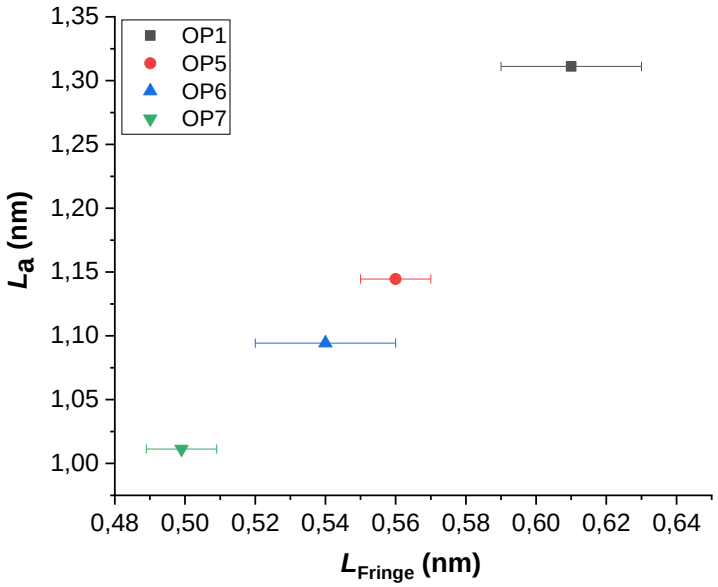

Fig. 8: Correlation of L_a obtained from Raman spectra and fringe length from HRTEM [21].

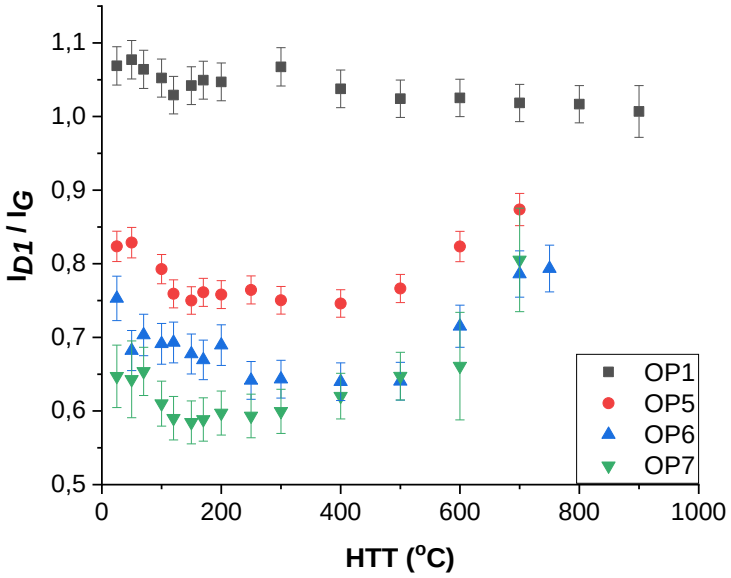

Fig. 9: The evolution of I_{D1}/I_G ratio in Raman spectra of the miniCAST soot vs. heat treatment temperature (HTT).

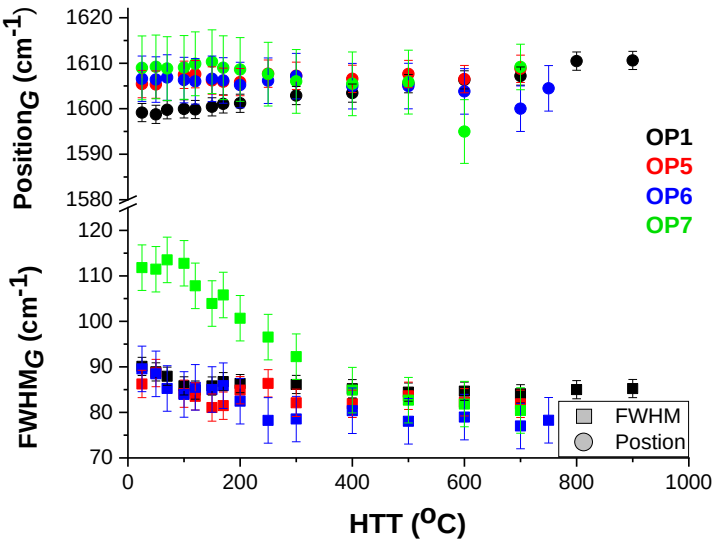

Fig. 10: Positions and FWHM of G peak as a function of HTT